

To appear in ApJ

A Powerful Radio Halo in the Hottest Known Cluster of Galaxies 1E0657–56

H. Liang

Physics Department, University of Bristol, Tyndall Avenue, Bristol, BS8 1TL, UK

h.liang@bristol.ac.uk

R. W. Hunstead

School of Physics, University of Sydney, NSW 2006, Australia

rwh@physics.usyd.edu.au

M. Birkinshaw

Physics Department, University of Bristol, Tyndall Avenue, Bristol, BS8 1TL, UK

Mark.Birkinshaw@bristol.ac.uk

and

P. Andreani

Dip. di Astronomia, Università di Padova, Vicolo Osservatorio 5, I-35122, Padova, Italy

andreani@pd.pd.astro.it

ABSTRACT

We report the detection of a diffuse radio halo source in the hottest known cluster of galaxies 1E0657–56 (RXJ0658–5557). The radio halo has a morphology similar to the X-ray emission from the hot intracluster medium. The presence of a luminous radio halo in such a hot cluster is further evidence for a steep correlation between the radio halo power and the X-ray temperature. We favour models for the origin of radio halo sources involving a direct connection between the X-ray emitting thermal particles and the radio emitting relativistic particles.

Subject headings: galaxies: clusters: individual (1E0657–56 (RXJ0658–5557)) — galaxies: intergalactic medium — cosmology: cosmic microwave background — radio continuum: general — X-rays: general — techniques: interferometric — radiation mechanisms

1. INTRODUCTION

Diffuse cluster radio sources are found in a few X-ray luminous clusters of galaxies. They are extended (~ 1 Mpc), have low surface brightnesses, and exhibit steep spectra ($\alpha \leq -1$, $S_\nu \propto \nu^\alpha$). They cannot be identified with any one individual galaxy but are associated with the cluster as a whole. Diffuse cluster radio sources are generally separated into two classes: halos and relics. Halos are centred on the X-ray emission (e.g. Coma-C is a proto-type radio halo source; Giovannini et al. 1993) whereas relics are peripheral and exhibit stronger polarisation than halos (e.g. A3667 has a large relic; Röttgering et al. 1997). In this paper, we will concentrate on halo sources.

Until recently, systematic surveys for radio halo sources found few examples, with the total number of known halos being ~ 5 (Feretti & Giovannini 1996). They are thus considered to be rare, and owing to their small number remain a poorly understood class of radio sources even though the first example, Coma-C, was discovered over 20 years ago. The spectra suggest that halo radio emission arises predominantly by the synchrotron process. However, the formation of radio halos remains a puzzle: why do they occur in some clusters and not in others, and what is the origin of the magnetic field and relativistic particles?

A number of models have been proposed to explain the formation of radio halos (e.g. Jaffe 1977; Dennison 1980; Roland 1981). Most of these early models suggest that ultra-relativistic electrons originate either as relativistic electrons from cluster radio sources re-accelerated by in-situ Fermi processes or turbulent galactic wakes, or as secondary electrons produced by the interaction between relativistic protons (again from cluster radio galaxies) and thermal protons. However, the energetics involved are problematic and the models could not always fit the observations (e.g., see review by Böhringer 1995). Harris et al. (1980) first suggested that radio halos are formed in cluster mergers where the merging process creates the shocks and turbulence necessary for the magnetic field amplification and high energy particle acceleration. More recently, Tribble (1993) showed that the energetics involved in a merger are more than enough to power a radio halo. The halos thus produced are expected to be transient since the relativistic electrons lose energy on time scales of $\sim 10^8$ yrs and the time interval between mergers is of order $\sim 10^9$ yrs. This argument was used to explain why radio halos are rare.

In this paper, we will describe the properties of the radio halo found in one of the hottest known clusters 1E0657–56, and suggest a new model for the origin of cluster halos based on the radio and X-ray properties of all 10 confirmed halos. §2 describes the multi-wavelength properties of cluster 1E0657–56; §3 describes the radio observations; §4 discusses the radio properties of the halo found in 1E0657–56; and §5 discusses the origin of radio halos. Throughout the paper we will use $H_0 = 50 \text{ km s}^{-1} \text{ Mpc}^{-1}$, $q_0 = 0.5$ and $\Lambda_0 = 0$.

2. THE CLUSTER 1E0657–56

The cluster 1E0657–56 was originally found in the Einstein slew survey (Tucker et al. 1995), and subsequent optical observations confirmed it to be a rich cluster at $z \sim 0.296$ with a velocity dispersion of $1213^{+352}_{-191} \text{ km s}^{-1}$ (Tucker et al. 1998). It has high X-ray luminosity and was shown to be one of the hottest known clusters by Tucker et al. (1998).

2.1. X-ray Properties

The cluster was observed for 25 ksec by ASCA in 1996 May and with the ROSAT High-Resolution Imager (HRI) in 1995 for 58 ksec (Tucker et al. 1998). Tucker et al. (1998) analysed the ASCA Gas Scintillation Imaging Spectrometers (GIS) and Solid-state Imaging Spectrometers (SIS) data and found the cluster to have a best fit temperature of $kT_x \sim 17.4 \pm 2.5 \text{ keV}$ and a bolometric luminosity of $L_{bol} \sim (1.4 \pm 0.3) \times 10^{46} \text{ erg s}^{-1}$. However, Yaqoob (1999) challenged these results by re-analysing the ASCA GIS/SIS data and arrived at a temperature of $\sim 11\text{--}12 \text{ keV}$, abundance $A \sim 0.2$ solar, and a neutral hydrogen absorption column density $N_H \sim 15 \times 10^{20} \text{ cm}^{-2}$, much higher than the Galactic value. Yaqoob found that the only way to reproduce the high temperature deduced by Tucker et al. (1998) was to fix the neutral hydrogen column density to the Galactic value, and concluded that fixing the absorption column density in such a way leads to an artificially high temperature.

Since then, some ROSAT Position-Sensitive Proportional Counter (PSPC) data have become publicly available. Since it is known that ASCA SIS data below 1 keV suffer from inaccurate calibration, we re-estimate the cluster temperature by fitting to the combined ASCA GIS and ROSAT PSPC data. The GIS and PSPC data complement each other: the GIS is more sensitive to the cluster temperature while the PSPC is more sensitive to the soft X-ray absorption.

We followed the standard ASCA procedure for screening the GIS2 and GIS3 data as set out in *The ABC guide to ASCA data reduction*¹. The spectra were extracted from a circular region of radius $7.25'$ centred on the cluster, after the subtraction of a local background, extracted from the same frame in areas with no obvious emission. The spectra were regrouped to a minimum of 50 counts per bin. The XSPEC package² (Arnaud 1996) was used to fit the GIS spectra between 0.8 and 10 keV by a Raymond-Smith spectrum (Raymond & Smith 1977), with fractional solar relative abundances from the table of Feldman (1992) and photoelectric absorption (Morrison & McCammon 1983). Temperature, abundance A , absorption (parametrised by N_H), and the normalisation were taken as free parameters. The best fit was $kT_x \sim 15.6^{+3.1}_{-2.3} \text{ keV}$, $N_H \sim (2.2^{+3.9}_{-2.2}) \times 10^{20} \text{ cm}^{-2}$, and $A \sim 0.49 \pm 0.27$ with a reduced $\chi^2 \sim 1.03/\text{d.o.f.}$. The errors correspond to 90% confidence

¹<http://heasarc.gsfc.nasa.gov/docs/asca/abc/abc.html>

²http://legacy.gsfc.nasa.gov/docs/xanadu/xspec/u_manual.html

limit. It is clear that N_H is poorly constrained by the GIS data alone, as expected from the absence of low-energy data.

We retrieved from the ROSAT archive a 4.7 ksec-exposure PSPC event file observed in 1997 February. A spectrum of the X-ray emission from the cluster gas was extracted from the central 5' radius after the subtraction of discrete sources and background contributions. The background was estimated from an annulus between radii of 8–10' centred on the cluster. Only the spectrum within the energy range between 0.1 and 2.0 keV was used for model fitting.

A combined fit of a Raymond-Smith spectrum to the GIS and PSPC spectra gave the best fit as follows: $kT_x = 14.5_{-1.7}^{+2.0}$ keV, $N_H = (4.2_{-0.5}^{+0.6}) \times 10^{20}$ cm $^{-2}$, $A = 0.33 \pm 0.16$ (see Fig. 1) with a reduced $\chi^2 \sim 1.03$ /d.o.f.. A direct radio-astronomical measure of the Galactic neutral hydrogen column density towards 1E0657–56 gives $N_H \sim 5.8 \times 10^{20}$ cm $^{-2}$ (E. M. Arnal, private communication); Dickey & Lockman (1990) gives a value of 6.6×10^{20} cm $^{-2}$. Recently we have obtained a high resolution (16' beam) measurement of the Galactic neutral hydrogen column density towards 1E0657–56 using the Parkes telescope, giving a $N_H \sim 4.6 \times 10^{20}$ cm $^{-2}$ (C. Brüns, private communication) which is very close to the X-ray fitted value. Thus it appears that the temperature is lower than that estimated in Tucker et al. (1998), although 1E0657–56 is still one of the hottest known clusters. On the other hand, our best fit temperature is higher than that deduced by Yaqoob (1999) and our best fit N_H is much closer to the Galactic value than that given by Yaqoob. The difference is unlikely to be caused by different background subtraction techniques, since Yaqoob tried a wide range of background subtraction methods and found that the systematic differences between the various techniques are less than the statistical errors. We tested our result by fixing the N_H and abundance A at the values given by Yaqoob, and found a best fit $kT_x \sim 11.3 \pm 1.0$ keV, consistent with his result but with a high reduced χ^2 of 1.56/d.o.f.. Figure 2 shows that Yaqoob's fit (to the ASCA data alone) is inconsistent with the PSPC data which extend to lower energies (~ 0.1 keV) than the SIS (~ 0.5 keV), and are therefore more sensitive to soft X-ray absorption.

The HRI image of the cluster shows two clearly separated clumps (see Figure 5). Andreani et al. (1999) analysed the spatial distribution of the X-ray emission using the HRI data and found that the X-ray surface brightness can be fitted with two spherically symmetric β -models (Cavaliere & Fusco-Femiano 1976) with gas density distributions given by

$$n_e(\theta) = n_{e,0} \left[1 + \left(\frac{\theta}{\theta_c} \right)^2 \right]^{-3\beta/2}, \quad (1)$$

where $\beta = 0.7, 0.49$, $\theta_c = 1.23', 0.26'$ and $n_{e,0} = 0.0063, 0.015$ cm $^{-3}$ for the eastern and western clumps respectively.

2.2. Sunyaev-Zel'dovich Effect

The Sunyaev-Zel'dovich effect (SZ effect) is the distortion of the blackbody spectrum of the Cosmic Microwave Background (CMB) due to inverse Compton scattering of CMB photons by free

electrons in a plasma such as an intracluster medium (Sunyaev & Zel'dovich 1972). The cluster 1E0657-56 was selected as a candidate for the detection of the SZ effect in the 1994–95 Swedish ESO Submillimeter Telescope (SEST) campaign (Andreani et al. 1999). The SEST observations show a $\sim 4\sigma$ detection of the SZ effect at 1.2 mm (~ 150 GHz) and a $\sim 3\sigma$ detection at 2 mm (~ 250 GHz) (Andreani et al. 1999). By combining the SEST results at 2mm with the X-ray surface brightness and temperature results (assuming an isothermal $kT_x \sim 17$ keV), Andreani et al. (1999) deduced a Hubble constant of $H_0 = 53_{-28}^{+38} \text{ km s}^{-1} \text{ Mpc}^{-1}$.

Shortly after the SEST observations, we obtained data with the Australia Telescope Compact Array (ATCA) at 8.8 GHz to confirm the SEST detection of the SZ effect. The ATCA observations were conducted using the special 210-m array which proved to be an excellent configuration for detecting low surface brightness diffuse emissions. The 4.9 and 8.8 GHz observations show complex radio source structures, including at least two extended, diffuse sources and an unusual strongly polarised ($P \sim 60\%$ at 8.8 GHz) steep spectrum ($\alpha \sim -1.9$) source (Liang et al., 2000, in preparation). The diffuse radio sources make the detection of the SZ effect difficult since the SZ effect is also extended and the straightforward point-source subtraction technique fails. However, since the radio sources in the cluster are interesting in their own right, we obtained further radio data. It was these later observations that led to the detection of a radio halo source.

3. RADIO OBSERVATIONS

3.1. ATCA Data

The ATCA has five 22-m antennas on a 3-km east-west rail-track and a sixth antenna 3 km from the western end of the track, giving baselines up to 6 km. Simultaneous observations were made in two frequency bands each of bandwidth 128 MHz divided into 32 frequency channels. The cluster 1E0657–56 was observed at 1.3, 2.4, 4.9, 5.9, and 8.8 GHz in several antenna configurations, so that similar uv coverage was obtained at all frequencies. Table 1 gives a summary of all the radio observations. The primary flux calibrator PKS B1934–638 was observed at least once a day and the phase calibrator PKS B0742–56 was observed every ~ 20 min. The data were calibrated with the MIRIAD package³ (Sault et al. 1995).

A radio halo source was clearly detected in maps with resolution $\sim 60''$ in all frequencies (see Fig. 3). A high resolution 1.3 GHz image of the cluster field is shown in Fig. 4a, where we see the halo source at the cluster centre, a possible relic source to the east, and a number of tailed sources on the periphery.

³<http://www.atnf.csiro.au/computing/software/miriad/userhtml.html>

3.2. MOST Data

The Molonglo Observatory Synthesis Telescope (MOST) is an east-west synthesis array comprising two collinear cylindrical paraboloids each 11.6 m wide by 778 m long, separated by a 15 m gap (Mills 1981, Robertson 1991). The telescope operates at 843 MHz, with a detection bandwidth of 3.25 MHz, and forms a comb of 64 real-time fan beams spaced by $22''$, which are interlaced to a spacing of $11''$. The synthesized beam-width is $43'' \times 43'' \text{cosec}|\delta| \text{ FWHM}$ (RA \times Dec). The observations of 1E0657–56 were made as part of the Sydney University Molonglo Sky Survey (SUMSS, Bock et al. 1999), in which the pointing of the beam set was time shared among seven adjoining positions to give a field size of $164' \times 164' \text{ cosec}|\delta|$. The background noise in this 12-hour image was 1.1 mJy rms and the reduction followed the standard survey pipeline. For comparison with the ATCA images, the MOST image in Fig. 3a was convolved out to a $60''$ circular beam.

4. A RADIO HALO IN 1E0657–56

4.1. Subtraction of Discrete Sources

In order to obtain a high-quality image of the diffuse radio halo and estimate its total integrated flux density, it is necessary to separate the emission from discrete sources embedded in the halo.

One way of estimating the flux density of discrete sources is to make a high resolution image using only the long baseline data ($> 5000\lambda$) that is unlikely to contain any signal from the diffuse halo emission. This image, which has a synthesized beam FWHM $\sim 6''$, is then deconvolved using the CLEAN algorithm. Fig. 4 shows the image made from all the 1.3 GHz data and the image from the long-baseline data with only sources within the halo region restored. The clean components of discrete sources embedded in the halo are then subtracted from the visibility (or uv) data set. These sources, marked in Fig. 4b, are unresolved with the exception of two sources (A,C) which were slightly extended. The flux densities of these discrete sources at various frequencies are listed in Table 2. A radio image of the halo at 1.3 GHz, with these embedded discrete sources subtracted, is shown in Fig. 5a & 5b.

4.2. Halo Total Flux Density

Estimation of the total flux density of a diffuse source is rather difficult, even after solving the problems of separating discrete sources from the diffuse emission (§4.1). The difficulty is two-fold: firstly, we need to define the angular size of the emission, which depends on the noise level in the image; and secondly, we need to know if we have sampled a large enough angular scale (i.e. short enough baselines) to include all the flux density. In the following paragraphs we describe two independent methods of estimating the integrated flux density as a function of the area of integration.

First, we make a low resolution image ($\sim 60''$ beam) using the uv data-set that has the discrete sources already subtracted, but taking only the short-baseline data ($< 3600\lambda$). This ensures that the data used for the estimation of the halo flux density are independent of the long-baseline data used for the subtraction of discrete sources. The integrated flux density of the halo estimated from such an image is plotted as a function of the area of integration in Fig. 6 (open circles). While the low resolution of the image ensures relatively high brightness sensitivity, the area of integration is limited because of blending with extended sources near the halo, a problem made worse by the large beam size (see Fig. 4a).

We now examine an alternative method of estimating the total halo flux density which also serves as a check on the method above. We integrate the signal within increasing regions of the halo on the high resolution image (Fig. 4a) which uses all the data and has not undergone source subtraction. The flux densities of the sources embedded in these regions are estimated from the image in Fig. 4b (see Table 2) and subtracted from the integrated flux density, giving the open triangles shown in Fig. 6. By careful exclusion of extended sources in or near the halo, the halo can be integrated over a larger area. In the first method (open circles in Fig. 6) the largest area of integration corresponds to region ‘1’ marked in Fig. 4b. The largest area used in the second method (open triangles) corresponds to the full extent of the X-ray emission less the regions of other extended sources. The smallest region in Fig. 6 corresponds to region ‘2’ in Fig. 4b.

Fig. 6 shows that the two methods agree and that the halo emission extends over a region at least 3.5 Mpc^2 in area with a total flux density of $78 \pm 5 \text{ mJy}$ at 1.3 GHz, which corresponds to a rest frame 1.4 GHz power of $(4.3 \pm 0.3) \times 10^{25} \text{ W Hz}^{-1}$. This power is likely to be a lower limit since there are negative contours around the halo in the 1.3 GHz image (Fig. 3b), which we interpret as evidence of missing short spacings. Further ATCA observations in the 210-m configuration are needed to study better the outer parts of the halo. With a power $P_{1.4} \sim 4.3 \times 10^{25} \text{ W Hz}^{-1}$, and a largest linear extent $\sim 2 \text{ Mpc}$, the radio halo source in 1E0657–56 is the strongest and largest known.

4.3. Correction for the SZ Effect

As mentioned in §2.2, this cluster shows a relatively strong SZ effect which produces a decrement at centimetre wavelengths and is also cluster-wide and diffuse. It is thus difficult to separate the SZ effect from the halo emission using the radio data alone. However, the SZ effect is strong enough at 4.9, 5.9 & 8.8 GHz to cause a significant underestimate of the radio halo flux density and an apparent steepening of the spectrum.

To obtain a reliable radio spectrum for the halo, we need to correct for the SZ effect at each frequency. We simulate the SZ effect at 4.9 to 8.8 GHz, using the X-ray data and the SEST detection at 2 mm. Andreani et al. (1999) found that the SZ effect detected at 2 mm was consistent with a model of the X-ray surface brightness expressed by two β -models (corresponding to the two X-

ray clumps) assuming an isothermal gas temperature of ~ 17 keV, if $H_0 \sim 50 \text{ km s}^{-1} \text{ Mpc}^{-1}$. For consistency with the SEST results, we use this gas temperature only for these calculations; in the rest of the paper, we use the newly-derived gas temperature given in §2.1. Since the SEST results provide no structure information for the gas, we have to use the X-ray derived gas parameters, i.e. $n_{e,0}, \theta_c, \beta$ from Andreani et al. (1999; or see §2.1), to simulate an SZ effect image at each frequency. This simulated SZ effect image is then weighted by the primary beam of the ATCA, Fourier transformed, and subtracted from the uv data-set at that frequency. The image obtained from the resulting uv data-set contains only the radio emission from the halo and can be analysed as in §4.2 to get the halo flux densities. Fig. 7 shows the halo flux density in a specific region at various frequencies before and after the correction for the SZ effect, indicating a substantial difference at high frequencies.

4.4. Radio Spectrum

To obtain the spectral index of the halo, we took data from the inner uv-plane (baselines $< 3600\lambda$) for each available frequency. The observations were planned such that roughly the same region in the uv-plane was sampled at the various frequencies. The data were tapered such that the synthesized beam FWHM was $\sim 60''$ at each frequency. The images are shown in Fig. 3. To form a spectrum, the same area of integration was used at each frequency and methods in §4.1 & §4.2 were used to correct for small-angular-size radio sources and the SZ effect. The areas were selected to include only regions of obvious emission at all frequencies. The radio spectrum between 1.3 and 8.8 GHz for region ‘2’ marked in Fig. 4b is shown in Fig. 7 (dots). Determination of the spectral index from region ‘2’ is complicated since it includes three point sources (B, D & E) and an extended source (A, see Fig. 4b). The three point sources are detected only in the 1.3 GHz image. We can obtain the flux density of the extended source (A) from images like that of Fig 4b at each frequency and subtract them from the total integrated flux. The resulting spectral index of region ‘2’ is ~ -1.2 between 1.3 and 4.9 GHz, and ~ -1.3 between 2.4 and 8.8 GHz, indicating no significant steepening of the spectral index between 1.3 and 8.8 GHz.

We use the data from MOST to extend the spectrum to lower frequencies. The MOST images were produced by a real-time FFT and are thus fixed in resolution, excluding the possibility of subtracting the discrete sources embedded in the halo. We can only form a spectrum for the central part (region ‘3’) of the halo that is devoid of discrete sources. The ATCA data at various frequencies were tapered such that the final resolution would match the MOST resolution of $51'' \times 43''$ ($\text{PA} = 0^\circ$). The spectrum of region ‘3’ is shown by the triangles in Fig. 7. The spectrum can be fitted with a power law with a spectral index of -1.4 ± 0.1 using a least squares fit. In comparison, the average spectral index for the larger region (region ‘2’) is $\sim -1.3 \pm 0.1$. There is no evidence of any steepening of the spectral index in the outer regions compared with the central region (unlike what is observed in the Coma cluster Giovannini et al. 1993). The areas of the regions ‘3’ and ‘2’ marked in Fig. 4b are 0.14 Mpc^2 and 0.78 Mpc^2 respectively.

4.5. Polarisation

The ATCA measures all components of linear polarisation, and takes account of the polarisation leakage terms in the calibration of the data by the MIRIAD package.

Polarised emission was not detected for the radio halo source. We obtain an upper limit for linearly polarised emission at 1.3 GHz of 20%, 6.5%, and 1.4% at resolutions of 10'', 20'', and 60'' (corresponding to linear sizes of 55, 110, and 327 kpc) respectively. The upper limit was calculated as $\sqrt{(Q^2 + U^2)}/I$, where I was the Stokes I peak halo flux density and Q and U were the 3σ of the Stokes Q and U maps respectively. The polarisation upper limits obtained at higher frequencies were poorer, because of the steepness of the halo spectral index and consequent decrease in signal to noise of the data. So far polarisation has not been detected in any halo source.

4.6. Pressure & Energy

The total energy density, or pressure, is minimum when the energy density of the relativistic particles is close to the energy density of the magnetic field (Burbidge 1958). There is no strong physical justification for the particle and field energies to be in equipartition, but it has been conjectured that they maybe close to equipartition (Longair 1997). If we make this assumption, then we can calculate the minimum pressure of radiating electrons and magnetic fields in the halo source and compare it to the thermal pressure from the X-ray gas. We estimate the minimum pressure by following the procedure set out in Pacholczyk (1970), assuming a constant spectral index of ~ -1.3 between the cutoff frequencies of 10 MHz and 100 GHz, a emission volume filling factor ϕ of 1 and a ratio k between the energy in relativistic protons and electrons of 1. The minimum pressure of the radio plasma is a factor $\sim 10^4$ smaller than the thermal pressure. Since $P_{min} \propto \phi^{-4/7}(1+k)^{4/7}$, we need $k > 10^6$ for P_{min} to match the thermal pressure which seems unlikely. Similar results have been found in other radio halos (e.g. Feretti et al. 1997). Since the radio plasma interpenetrates the thermal gas, the radio and the thermal plasma each contributes a partial pressure to the total plasma pressure which appears to be dominated by the thermal pressure.

The total energy of the thermal plasma is $\sim 10^{63}$ ergs, and the energy in the relativistic plasma is $\sim 10^{60}$ ergs under conditions of equipartition (i.e. $B \sim 1\mu\text{G}$).

4.7. Morphological Structure

The radio halo is similar in extent and overall appearance to the cluster X-ray emission (see Fig. 5a). While Fig. 5a shows that the radio emission is enhanced at the main peak of the X-ray emission, Fig. 5b shows that the radio emission is also enhanced at the densest part of the optical galaxy distribution. On the whole the radio emission follows that of the optical galaxy distribution

more closely than the X-ray emission. This was also found in the Coma cluster (Kim *et al.* 1990). We will discuss this point further in §5.3.

The main concentration of galaxies is displaced from the dominant (eastern) peak of the X-ray emission (see Fig. 5c). Both the X-ray gas and the galaxy distribution suggest that the cluster is undergoing a merging process. Since the X-ray clumps are well separated, the merger appears to be in a relatively early stage. Since galaxies are more or less collisionless, but gas is collisional, a merger between two subclusters tends to allow the galaxies to stream past one another, while the gas tends to coalesce quickly. Fig. 5c shows that the galaxy clumps in 1E0657–56 are further apart than the gas clumps, indicating that the galaxies have crossed each other at least once. The projected merging axis appears to be close to the RA-direction. Shocks produced during the merger are a plausible source for the energy of the relativistic electrons responsible for the radio halo emission.

5. THE ORIGIN OF RADIO HALOS

5.1. Are Radio Halos Intrinsically Rare?

A number of surveys have been conducted to search for radio halos. The earliest were conducted at Green Bank at 610 MHz (Jaffe & Rudnick 1979), at metre wavelengths 50–120 MHz (Cane *et al.* 1981) and at Arecibo at 430 MHz (Hanisch 1982), but yielded few examples. Most of the surveys selected either nearby Abell clusters (Hanisch 1982), or clusters with known X-ray emission or radio sources. More recently, Lacy *et al.* (1993) imaged a sample of radio sources from the 8C 38 MHz survey (within 3.3° of the North Ecliptic cap) using the Cambridge Low Frequency Synthesis Telescope at 151 MHz but did not find any new halo sources.

Recent X-ray selected surveys of halos as well as observations aimed at detecting the SZ effect have found many more halo candidates suggesting that halos may not be as rare as they were once thought to be.

Moffet and Birkinshaw (1989) first suggested that there may be a correlation between the presence of an SZ effect and a radio halo source, since the only three clusters A2218, A665, and CL0016+16 which had an SZ effect detected at the time also had extended diffuse radio emission. One of the strongest radio halos was found in A2163 in an attempt to detect the SZ effect (Herbig & Birkinshaw 1994). Among the seven clusters observed at the ATCA for the SZ effect, two show clear evidence of a radio halo (A2163, 1E0657–56), while another three show faint extended emission which may be either the result of the blending of discrete radio sources or a faint halo (Liang 1995). It is perhaps not surprising that searches for the SZ effect have been good at finding halo sources: the SZ effect is also cluster-wide, thus diffuse and extended like the halo sources. Any observation designed to search for the SZ effect will optimise the brightness sensitivity and thus favour the detection of halos. If, in addition, there is a physical mechanism that associates hot,

luminous, X-ray emitting atmospheres and radio halos, searches for SZ effects which target such clusters would be expected to find radio halos frequently.

Giovannini et al. (1999a), in their correlation of NVSS images with the catalogue of X-ray Brightest Abell Clusters (XBAC; Ebeling et al. 1996), found 13 candidates for diffuse radio halos. They noticed a significant increase in the percentage of diffuse radio sources in high luminosity clusters compared with low luminosity clusters: 27–44% in clusters with $L_x > 10^{45}$ erg/s as compared with 6–9% for $L_x < 10^{45}$ erg/s.

We conclude that radio halos are not intrinsically rare, and appeared to be rare from the results of early surveys partly because of the difficulty of detecting such low surface brightness objects and partly because of the selection criteria.

5.2. The Link between Thermal and Relativistic Electrons

While Giovannini et al. (1999a) found more halos in high than low X-ray luminosity clusters, they did not find a correlation between their radio power and the cluster X-ray luminosity. Here we plot the rest frame 1.4 GHz radio power ($P_{1.4}$) against the cluster X-ray luminosity (L_x) for only well-confirmed radio halos (not relic sources) using the best radio data available for each halo. Fig. 8 shows that there is a correlation between radio and X-ray luminosities for $L_{(0.1-2.4)keV} > 10^{45}$ ergs s^{-1} clusters contrary to Giovannini et al. (1999a) where they plotted all candidate halos using the radio power obtained from the NVSS for each halo. Instead of plotting radio power against X-ray luminosity, we examine the relationship between halo radio power and cluster X-ray temperature. Fig. 9 shows the 1.4 GHz integrated radio power of cluster halos plotted against the cluster temperature, demonstrating a steep correlation. Since only well-confirmed radio halos are plotted, the sample of clusters shown is by no means complete. The apparent rareness of halos can be explained by the steepness of the relationship shown in Fig. 9: only clusters with a high X-ray temperature at moderate redshifts are easily detectable. The surface brightness of halos decreases with increasing redshift at least as fast as $(1+z)^5$ when taking account of the K-correction, thus the halo surface brightness rapidly diminishes with increasing redshift. On the other hand, halos at low redshift are also difficult to detect since they tend to be resolved out in simple interferometric maps (or single dish observations without a large beam-throw).

In the 3 well-imaged cluster halos (Coma, A2163 & 1E0657–56), the extent and shape of the radio halo follows closely that of the cluster X-ray emission (Fig. 5; Deiss et al. 1997; Herbig & Birkinshaw in preparation). Both the correlation shown in Fig. 8 & 9 and the similarities between the radio and X-ray morphology indicate a direct connection between the thermal particles and the relativistic electrons responsible for the radio emission.

5.3. Formation of Radio Halos

We favour a model for radio halos where thermal electrons in the ICM provide the seed particles for acceleration to the ultra-relativistic energies necessary for synchrotron radiation (Liang 1999, Brunetti et al. 1999 & Schlickeiser et al. 1987). This differs from the early theories (e.g. Jaffe 1977) where the seed electrons diffused out of radio galaxies. In the past, the possibility of accelerating thermal electrons to relativistic energies has been dismissed, usually with little justification. We will examine this issue by looking at the arguments put forward against the possibility of accelerating thermal electrons to relativistic energies. One of the simple arguments was that such a process would be present in every cluster and thus fail to explain the perceived rarity of halos (Giovannini et al. 1993). As discussed earlier, such an argument does not necessarily hold: the strength of halos appears to be strongly related to the temperature of the thermal gas, and halos may be in every cluster and be detectable or not according to their brightness. Since high temperature clusters are relatively uncommon, so are powerful halos, but high-temperature clusters are likely to contain halos.

A second argument against the “thermal pool” origin of the ultra-relativistic electrons was that stochastic processes such as Alfvén, turbulent and shock acceleration are only efficient in accelerating electrons that are already mildly relativistic (e.g. Eilek & Hughes 1991 and references therein). This means that either the seed electrons are mildly relativistic already, or an injection process is necessary to create a substantial suprathermal tail in the electron energy distribution. To circumvent the injection process (not yet understood), it is attractive to invoke models that use the already-relativistic electrons from radio galaxies as seed particles to be re-accelerated.

However, observationally, it has also been shown that while halo candidates were found in nearly 30% of the high X-ray luminosity clusters in a survey for radio halo sources, none was found in the 11 clusters selected by the existence of at least one tailed radio source within 0.1 Abell radius (Giovannini et al. 1999b). This is further evidence that the relativistic electrons are more likely to have originated from the thermal pool of electrons than the radio galaxies: the appearance of halos is more closely linked to thermal X-ray emission than the presence of tailed radio galaxies.

A closer examination of the argument for an injection process show that it may not always be necessary in a cluster environment. According to Eilek & Hughes (1991), cyclotron resonance is responsible for the acceleration of electrons by Alfvén waves, and higher energy particles resonate with lower frequency waves. Since Alfvén waves have frequencies less than the ion gyrofrequency ($\Omega_p = eB/(m_p c)$), electrons need a minimum energy to be accelerated by Alfvén waves. This threshold energy can be calculated by substituting the ion gyrofrequency Ω_p and the dispersion relation into the equation for cyclotron resonance: $\omega - k_{\parallel}v_{\parallel} + \Omega_e/\gamma = 0$, where ω is the wave frequency, $k_{\parallel} = k \cos \phi$ and $v_{\parallel} = v \cos \theta$ are the components of the wave-number and particle velocity parallel to the magnetic field, and Ω_e/γ is the relativistic electron gyrofrequency. In the low-amplitude limit the waves are non-compressive, and the dispersion relation is given by (Krall

& Trivelpiece 1973)

$$\frac{\omega^2}{k^2} = \frac{v_A^2 \cos^2 \phi}{1 + v_A^2/c^2}, \quad (2)$$

where $v_A = B/\sqrt{4\pi m_p n_e}$ is the Alfvén speed. Hence the minimum energy or Lorentz factor required for an electron to be accelerated by Alfvén waves is given by

$$\gamma_{min} = \frac{m_p}{m_e} \left(\frac{v_A}{\eta c} \right)^2 + \frac{v_A}{\eta c} \sqrt{\left(\frac{m_p}{m_e} \right)^2 + \left(\frac{\eta c}{v_A} \right)^2}, \quad (3)$$

where $\eta = \cos \theta$. This threshold electron energy is already mildly relativistic (> 100 keV) in the limit of $(\eta c/v_A)^2 < (m_p/m_e)^2$, i.e. $n_e < (2 \times 10^{-4}/\eta^2)(B/\mu G)^2 \text{ cm}^{-3}$. However, in a high density environment, γ_{min} is close to one and thermal electrons can be accelerated by Alfvén waves. The environments of radio galaxies, including clusters, were considered to be of low density since the magnetic field strength B was thought to be a few μG , which means the density threshold is higher than the densities of most clusters.

Recent hard X-ray results from Beppo-SAX and Rossi-RXTE for Coma and other clusters have shown the magnetic field to be $B \sim 0.2\mu\text{G}$ if the excess hard X-ray emission is due to inverse Compton scattering of relativistic electrons by the CMB (e.g. Fusco-Femiano et al. 1999; Rephaeli et al. 1999; Valinia et al. 1999). Thus the density threshold is now $\sim 8 \times 10^{-6}/\eta^2 \text{ cm}^{-3}$, which makes most parts of clusters high density environments. For example, in the centres of clusters where $n_e \sim 10^{-3}$, the minimum energy required is just a few keV, and in the outer parts of a cluster where $n_e \sim 10^{-4}$ the minimum energy is still just a few tens of keV. Electrons with energies of a few tens of keV are readily available in intracluster plasma of hot clusters. Therefore, it is possible to accelerate thermal electrons in clusters through resonance with Alfvén waves. Further, Dogiel (1999) has shown that it is possible to produce a substantial suprathermal tail in the electron energy distribution through second order Fermi acceleration in cluster environments, so that additional seed electrons are naturally present in clusters without involving injection from radio galaxies.

On the one hand, the higher the X-ray luminosity of a cluster, the higher the density of thermal electrons; and on the other hand, the higher the X-ray temperature of a cluster, the higher the fraction of high energy electrons. These two effects multiply to increase the number of electrons above a threshold energy for efficient acceleration processes.

Both merging activity and the electron temperature may be responsible for the production of radio halos. A possible scenario would be that the initial merging activity provides the energy for accelerating electrons from the suprathermal tail of the energy distribution (where the hotter clusters have more power) to ultra-relativistic energies. Since cluster magnetic field strengths are less than $3\mu\text{G}$, the dominant energy loss mechanism for relativistic electrons is inverse Compton scattering of the cosmic microwave background radiation. Thus the typical lifetime of an electron that emits at 1.4 GHz is $t_{age} \sim 8 \times 10^7 \sqrt{B/(1\mu\text{G})} (1+z)^{-9/2} \text{ yr}$. If we assume a magnetic field of $B \sim 0.2\mu\text{G}$, then the lifetime of an electron that emits at 1.4 GHz in 1E0657–56 is $\sim 10^7 \text{ yr}$. After the shocks have disappeared, radio halos like that of 1E0657–56 may be maintained by in-situ electron acceleration in the residual turbulence. In the case of 1E0657–56, we found (Fig. 5)

that the radio halo emission is enhanced at the peak of the X-ray emission as well as that of the galaxy distribution. The enhancement of radio emission at the peak of the X-ray emission is naturally explained by our model where we expect the highest density of relativistic electrons at the density peak of the thermal electrons. We also expect that the galaxies streaming through the hot intracluster gas would maintain local turbulence and hence inject energy into the particles, producing enhanced radio emissions at the galaxy concentrations. Deiss & Just (1996) found through their calculations that it is possible to have turbulent velocities of several hundred km s^{-1} , which could considerably enhance the stochastic acceleration rates.

Cooling flow clusters are thought to be relaxed and devoid of merging activity. Most of the clusters shown in Fig. 9 are non-cooling flow clusters. This does not imply that mergers are the *critical* element in radio halo formation, since selection effects act to remove clusters from the sample in Fig. 9: cooling flow clusters are more likely to have significant central radio sources than non-cooling flow clusters (e.g. Peres et al. 1998). To our knowledge, no cluster with a strong cooling flow has been observed with sufficient dynamic range and surface brightness sensitivity to test whether or not it follows the $P_{1.4} - kT_x$ trend shown in Fig. 9. To illustrate the need for proper observations with high brightness sensitivities, we give as an example, RXJ1347-11, a strong cooling flow with the high gas temperature of $\sim 12.5 \text{ keV}$ (Allen & Fabian 1998) which has been observed by the NVSS with no obvious detection. However, the NVSS does not have enough brightness sensitivity to detect, in RXJ1347-11, a halo similar to that in 1E0657-56 because of the high redshift ($z \sim 0.45$) of the cluster (expected signal of $\sim 1.3 \text{ mJy}$ per $45''$ beam) and the high noise levels in the NVSS image ($\sim 0.5 \text{ mJy}$ per $45''$ beam).

6. CONCLUSIONS

We have found a powerful radio halo in the cluster 1E0657-56. At a rest frame 1.4 GHz radio power of $(4.3 \pm 0.3) \times 10^{25} \text{ W Hz}^{-1}$, it is one of the most powerful radio halo sources. It has a steep spectral index of $\alpha_{4864}^{1344} \sim -1.2$ typical of known halos. The brightness distributions of the radio halo and X-rays from the cluster gas are remarkably similar, suggesting a direct relationship between the ultra-relativistic electrons responsible for the synchrotron emission and the thermal intracluster gas. As further evidence for the radio/X-ray connection, we have found a steep correlation between the radio power of the halo and the X-ray temperature of the intracluster gas ($P_{1.4} - kT_x$) from the 10 confirmed cluster radio halos. We favour an explanation for the origin of radio halo sources, where the high energy tail of the thermal electron distribution is boosted to ultra-relativistic energies, thus providing a natural link between the halo radio power and X-ray gas temperature. Detailed calculations for such a model will be given in a future paper. Finally, it is important for our understanding of the origin of radio halo sources to establish the robustness of the $P_{1.4} - kT_x$ correlation by observing a temperature selected sample of clusters, and to test the mechanism by searching for halos in clusters with strong cooling flows but high temperature.

In addition, we have re-analysed the X-ray spectroscopic data using both ASCA GIS and

ROSAT PSPC data for 1E0657–56 and found the best fit temperature to be $kT_x = 14.5^{+2.0}_{-1.7}$ keV consistent with it being one of the hottest known clusters, as claimed by Tucker et al. (1998). The use of the PSPC data enabled us to determine the soft X-ray absorption to a better accuracy than previous results using ASCA data alone. We found the best fit neutral hydrogen column density to be consistent with the Galactic value given by radio-astronomical surveys, contrary to the much higher column density claimed by Yaqoob (1999) using ASCA data alone.

We are grateful to Sarah Maddison for help with the ATCA observations; Emilio Falco, Massimo Ramella and Wallace Tucker for providing the NTT image prior to publication; Christian Brüns and Lister Staveley-Smith for taking a H I measurement with Parkes Radio Telescope towards the cluster; and E. M. Arnal for providing 21cm measurements of the neutral Hydrogen column density from the IAR high sensitivity H I survey. H.L. would like to thank Ron Ekers for encouragement and helpful discussions, the ATNF for hospitality. The MOST is operated with the support of the Australian Research Council and the Science Foundation for Physics within the University of Sydney. The Australia Telescope is funded by the Commonwealth of Australia for operation as a National Facility managed by CSIRO. We would like to acknowledge the use of data from the HEASARC online service and the ROSAT public archive, and the use of the Karma package (<http://www.atnf.csiro.au/karma>) for the overlays.

REFERENCES

Allen S. & Fabian A., 1998, MNRAS, 297, 57

Andreani P. et al., 1999, ApJ, 513, 23

Arnal M., Bajaja E., Larrarte J.J., Morras R. & Poeppel W.G.L., 1999, submitted to A&AS

Arnaud A., 1996, in ASP Conf. Ser. 101, Astronomical Data Analysis Software and Systems V, ed. G.H. Jacoby & J. Barnes (San Francisco: ASP), 17

Böhringer H., 1995, Reviews in Modern astronomy, 8, 259

Bock D. C.-J., Large M. I. & Sadler E. M., 1999, AJ, 117, 1578

Brunetti et al., 1999, in Proceedings of the Ringberg workshop on Diffuse Thermal and Relativistic Plasma in Galaxy Clusters, ed. H. Boehringer, L. Feretti, & P. Schuecker (MPE report), astro-ph/9907125

Burbidge, G. R., 1958, ApJ, 129, 841

Cane H., Erickson W., Hanisch R. & Turner P., 1981, MNRAS, 196, 409

Cavaliere A. & Fusco-Femiano R., 1976, A&A, 49, 137

David L., Slyz A., Jones C., Forman W., Vrtilek S. & Arnaud K., 1993, *ApJ*, 412, 479

Deiss B., Reich W., Lesch H. & Wielebinski R., 1997, *A&A*, 321, 55

Deiss B. & Just A., *A&A*, 305, 407

Dennison B., 1980, *ApJ*, 239, L93

Dickey J. M. & Lockman F. J., 1990, *ARA&A*, 28, 21

Dogiel V., 1999, in *Proceedings of the Ringberg workshop on Diffuse Thermal and Relativistic Plasma in Galaxy Clusters*, ed. H. Boehringer, L. Feretti, & P. Schuecker (MPE report)

Ebeling H., Voges W., Böhringer H., Edge A., Huchra J. & Briel U., 1996, *MNRAS*, 283, 1103

Eilek J. & Hughes P., 1991, in *Beams and Jets in Astrophysics* (Cambridge Astrophysics Series), 428.

Elbaz D., Arnaud M. & Böhringer H., 1995, *A&A*, 293, 337

Feldman U., 1992, *Physica Scripta* 46, 202

Feretti L. & Giovannini G., 1996, in *IAU symposium 175, Extragalactic radio sources*, ed. R.D. Ekers, C. Fanti & L. Padrielli (Kluwer), 333

Feretti L., Giovannini G. & Böhringer H., 1997a, *New Astronomy* 2, 501

Feretti L., Böhringer H., Giovannini G. & Neumann D., 1997b, *A&A*, 317, 432

Fusco-Femiano R., et al., 1999, preprint, *astro-ph/9901018*

Giovannini G., Feretti L., Venturi T., Kim K.-T. & Kronberg P. P., 1993, *ApJ*, 406, 339

Giovannini et al., 1999a, preprint, *astro-ph/9904210*

Giovannini et al., 1999b, in *Proceedings of the Ringberg workshop on Diffuse Thermal and Relativistic Plasma in Galaxy Clusters*, ed. H. Boehringer, L. Feretti, & P. Schuecker (MPE report)

Hanisch R. J., 1982, *A&A*, 111, 97

Harris D. E., Kapahi V. K., & Ekers R. D., 1980, *A&AS*, 39, 215

Herbig T. & Birkinshaw M., 1994, *BAAS*, 185, 3307

Jaffe W., 1977, *ApJ*, 212, 1

Jaffe W. & Rudnick L., 1979, *ApJ*, 233, 453

Kim K.-T., Kronberg P. P., Dewdney P. E., & Landecker T. L., 1990, *ApJ*, 355, 29

Krall N. A. & Trivelpiece A. N., 1973, Principles of Plasma Physics, (New York: McGraw-Hill)

Lacy M., Hill G., Kaiser M. & Rawlings S., 1993, MNRAS, 263, 707

Liang H., 1995, Thesis, ANU

Liang H., 1999, in Proceedings of the Ringberg workshop on Diffuse Thermal and Relativistic Plasma in Galaxy Clusters, ed. H. Boehringer, L. Feretti, & P. Schuecker (MPE report), astro-ph/9907057

Longair M., 1997, High Energy Astrophysics, Vol. 2 (Cambridge University press)

Markevitch M., Forman W., Sarazin C. & Vikhlinin A., 1998, ApJ, 503, 77

Mills B. Y., 1981, Proc. Astron. Soc. Australia, 4, 156

Moffet A. & Birkinshaw M., 1989, AJ, 98, 1148

Morrison R. & McCammon D., 1983, ApJ, 270, 119

Pacholczyk A. G., 1970, Radio Astrophysics, (San Francisco: W. H. Freeman & Sons, Inc.)

Peres C., Fabian A., Edge A., Allen S., Johnston R. & White D., 1998, MNRAS, 298, 416

Pierre M., Matsumoto H., Tsuru T., Ebeling H. & Hunstead H., 1999, A&AS, 136, 173

Raymond, J. C., & Smith, B. W., 1977, ApJS, 35, 419

Reid A., Hunstead R., Lémonon L. & Pierre M., 1999, MNRAS, 302, 571

Rephaeli Y., Gruber D., & Blanco P., 1999, ApJ, 511, L21

Robertson J. G., 1991, Australian J. Phys., 44, 729

Roland J., 1981, A&A93, 407

Röttgering H., Wieringa M., Hunstead R. & Ekers R., 1997, MNRAS, 290, 577

Sault R. J., Teuben P. J., Wright M. C. H., 1995, in Astronomical Data Analysis Software and Systems IV, ASP Conf. Ser. 77, ed. R. Shaw, H.E. Payne, J.J.E. Hayes (San Francisco: ASP), 433

Schlickeisser, R., Sievers A. & Thiemann H., 1987, A&A, 182, 21

Sunyaev, R. A., & Zel'dovich Ya.B., 1972, Comm. Astr. Spa. Phys. 4, 173

Tucker W. H., Tananbaum H., Remillard A. A., 1995, ApJ, 444, 532

Tucker W. H., Blanco P., Rappoport S., David L., Fabricant D., Falco E.E., Forman W., Dressler A., Ramella M., 1998, ApJ, 496, L5

Tribble P., 1993, MNRAS, 263, 31

Valinia A. et al., 1999, ApJ, 515, 42

Yaqoob T., 1999, ApJ, 511, L75

Fig. 1.— X-ray spectra from the ASCA GIS and ROSAT PSPC. The observed spectra are shown with error bars. A Raymond-Smith thermal spectrum with $kT_x \sim 14.5$ keV, $A \sim 0.33$ solar and absorption $N_H \sim 4.2 \times 10^{20}$ cm $^{-2}$, convolved with instrumental responses, is shown as a histogram plot. A good fit to the data is obtained, with reduced χ^2 of 1.03/d.o.f.

Fig. 2.— X-ray spectra from the ASCA GIS and ROSAT PSPC, as in Fig. 1. The superimposed model spectra, shown as a histogram plot, arise from a Raymond-Smith thermal spectrum with $kT_x \sim 11.3$ keV, $A \sim 0.2$ solar and absorption $N_H \sim 15 \times 10^{20}$ cm $^{-2}$ after convolution with the instrumental responses. This model, consistent with the results of Yaqoob (1999) from ASCA data alone, is a poor fit, with a reduced $\chi^2 = 1.56$. The data require less soft X-ray absorption than in this model.

Fig. 3.— Low resolution radio images overlaid on grey scale PSPC hard-band (0.5–2.0 keV) image smoothed with a 50'' Gaussian: a) MOST contour image at 843 MHz smoothed to a beam size of 60''; b)-e) ATCA contour images with a 60'' beam at 1.3, 2.4, 4.9, 5.9, and 8.8 GHz respectively; only the shortest spacings ($< 3600\lambda$) are used. Contour levels are $(-3, 3, 6, 12, 24, 48, 96, 192, 384) \times \sigma$, where rms noise are $\sigma \sim 1100, 51, 110, 56, 65, 56\mu\text{Jy}/\text{beam}$ for frequencies of 0.8, 1.3, 2.4, 4.9, 5.9, and 8.8 GHz respectively.

Fig. 4.— a) A 1.3 GHz ATCA image towards 1E0657–56 at a resolution of 6.5'' \times 5.9'', using all the data (uniform weighting). The noise level in the image is $44\mu\text{Jy}/\text{beam}$. b) A 1.3 GHz image using only the long baseline data ($> 5000\lambda$) with only the CLEAN components within the marked region '1' restored (beam size 6''). The unresolved sources are marked by a circle and the two extended sources (A and C) are marked by the small areas that were used to integrate their total flux. The sources are marked by letters and the three regions marked from '1' to '3' correspond to regions used for total flux estimates.

Fig. 5.— a) A grey scale image of the radio halo at 1.3 GHz with resolution 24'' \times 22'' after the subtraction of catalogued sources (Table 2) is overlaid with a ROSAT HRI contour image smoothed with a Gaussian of 10'' width. The contour levels are 0.35, 0.45, 0.6, 0.8, 1.0, 1.2, 1.4, 1.6, 1.8, 2.0, 2.2 HRI cts/s. b) The same radio image in contours overlaid on a ESO New Technology Telescope (NTT) R-band image (courtesy of E. Falco and M. Ramella) with the same image scale as a). The radio contours are $(3, 6, 12, 18, 24) \times \sigma$, where the noise σ in the radio image is $90\mu\text{Jy}/\text{beam}$. c) The same HRI contours overlaid on the NTT R-band image.

Fig. 6.— Integrated diffuse halo flux density versus the area of integration. The open circles are integrated flux densities from an image made with a source-subtracted uv data-set and smoothed to 60'' resolution using only the short baseline ($< 3600\lambda$) data. The triangles are integrated flux densities from a high resolution image shown in Fig. 4a but with the embedded sources obtained from Fig. 4b subtracted afterwards. The error bars are 1σ errors.

Fig. 7.— Radio spectra from 0.843 GHz to 8.8 GHz of the cluster halo in 1E0657–56. The spectrum

of the central region (region 3 in Fig. 4(b)) is marked by triangles. For the larger region (region 2 in Fig. 4(b)) the spectrum is marked by circles. The filled data points have been corrected for the SZ effect. The uncorrected flux are represented as open symbols. The error bars are 1σ errors. The straight lines are the best least square fits to a power law spectrum.

Fig. 8.— Radio power $P_{1.4}$ at 1.4 GHz (rest frame) versus the cluster X-ray luminosity (0.1-2.4) keV for all the confirmed radio halo sources. Formal errors of $\sim 1\sigma$ are given for the halo power where it is known, in cases where the errors are not obviously stated in the literature, a 10% error is assumed. A 10% error is assumed for the X-ray luminosity. X-ray luminosities are obtained from Ebeling et al. 1996 and this paper. The radio powers are from Herbig & Birkinshaw in preparation, Reid et al. 1999, Giovannini et al. 1993, Feretti et al 1997a, 1997b, Giovannini et al. 1999a, Liang et al. in preparation and this paper.

Fig. 9.— Radio power $P_{1.4}$ at 1.4 GHz (rest frame) versus the cluster X-ray temperature kT_x for all the confirmed radio halo sources. The error bars for the intracluster gas temperature correspond to a 90% confidence limit. Formal errors of $\sim 1\sigma$ are given for the halo power where it is known, in cases where the errors are not obviously stated in the literature, a 10% error is assumed. The X-ray data are obtained from Allen & Fabian 1998, Markevitch et al. 1998, Pierre et al. 1999, Mushotzky & Scharf 1997, David et al. 1993 and this paper. The radio data are the same as in Fig. 8.

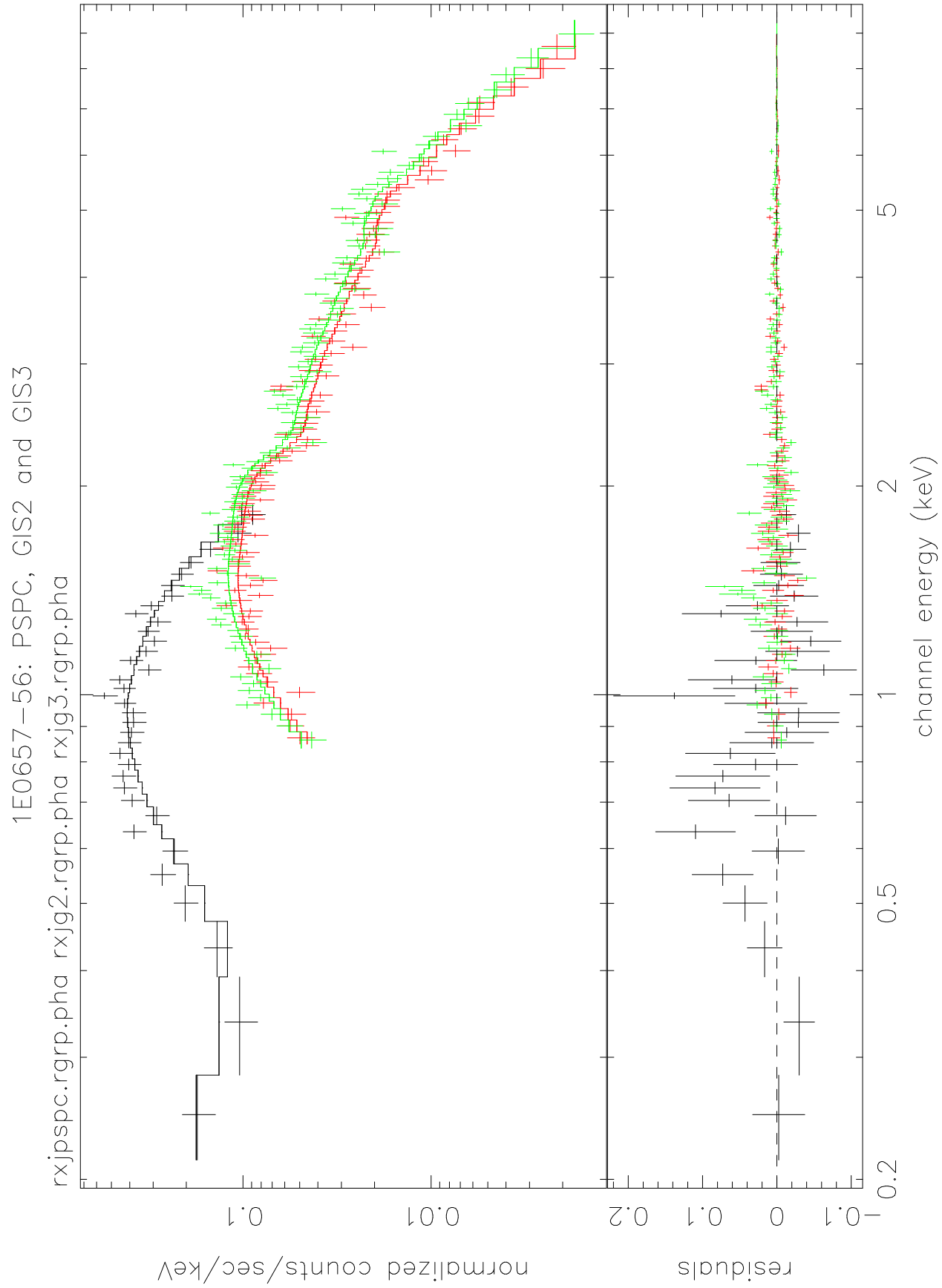
Table 1. Summary of Radio Observations

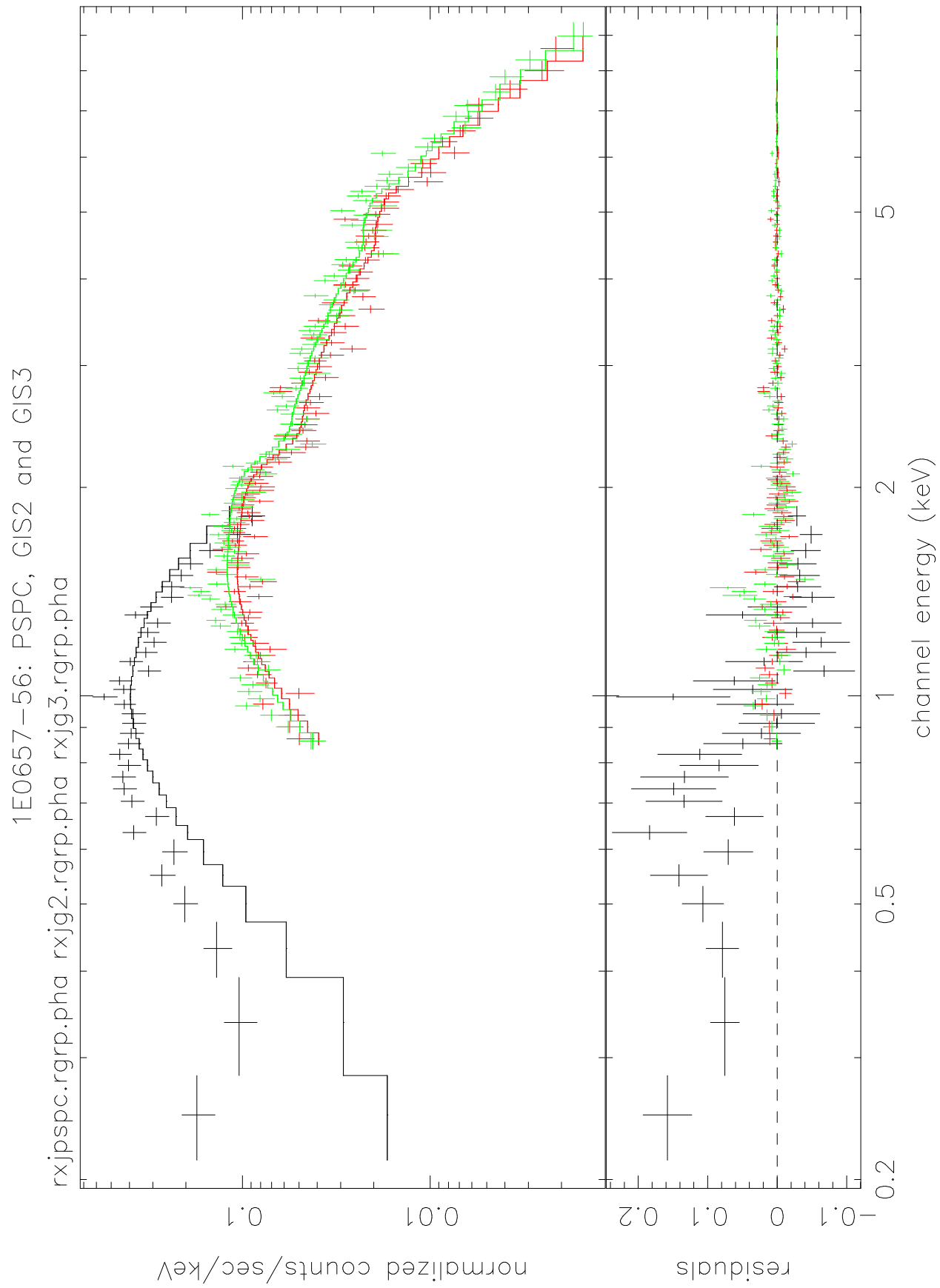
Date	Frequency (MHz)	Config.	Centre (J2000)						t_{obs} (hr)
			h	m	s	°	'	"	
Dec 1996	8768/8896	210	06	58	32.7	−55	57	19	56.6
	4800/4928	210	06	58	32.7	−55	57	19	11.2
	5824/5952	210	06	58	32.7	−55	57	19	11.4
May 1997	1344/2240	6B	06	58	32.7	−55	57	19	11.2
Jun 1997	1344/2240	750A	06	58	32.7	−55	57	19	10.0
Jul 1998	1344/2496	750E	06	58	32.7	−55	57	19	10.8
	8768/4800	750E	06	58	32.7	−55	57	19	9.7
Jan 1998	843	MOST	07	00	00.0	−56	35	24	12.0

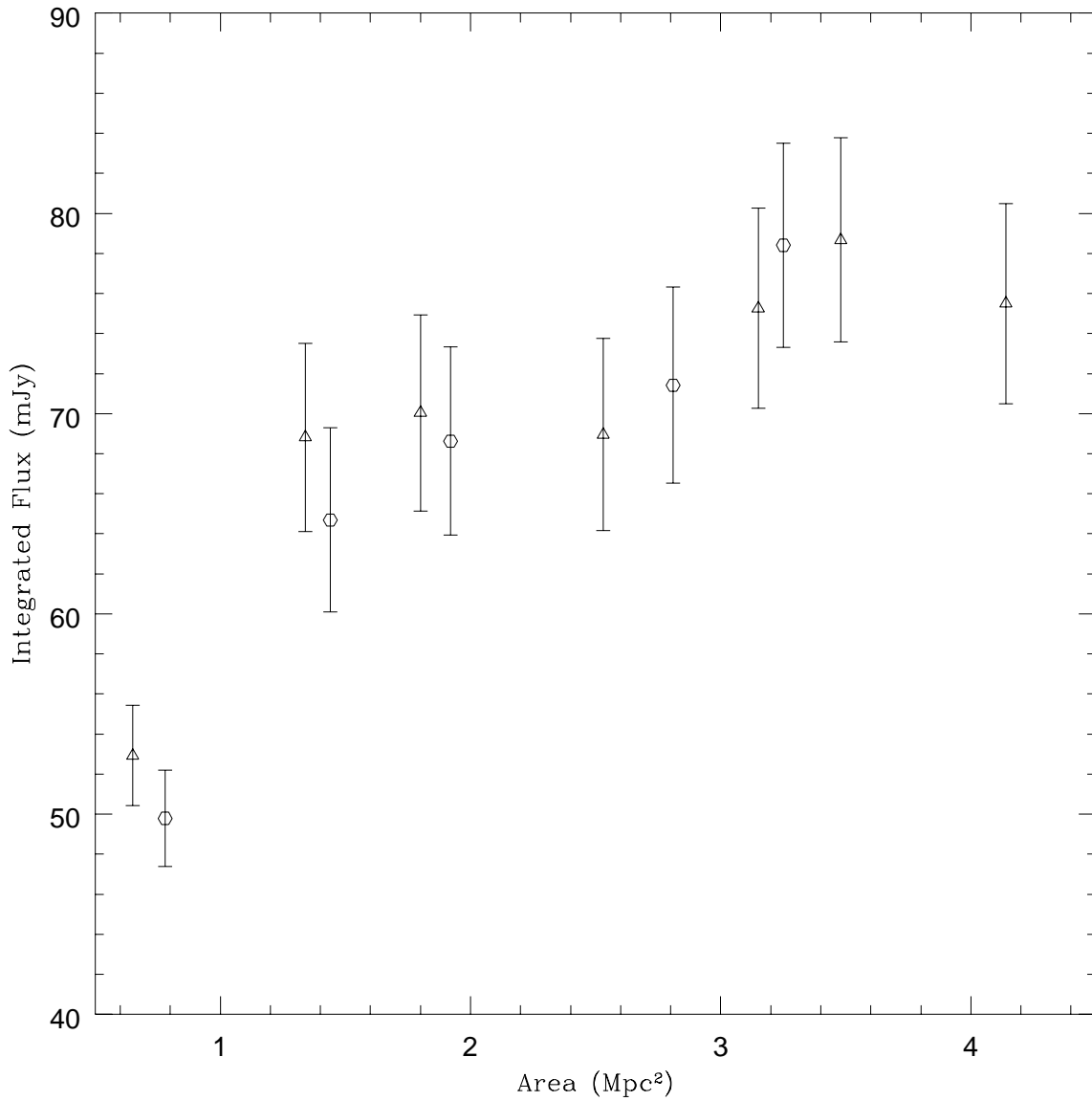
Table 2. Radio Flux Density of the Discrete Sources

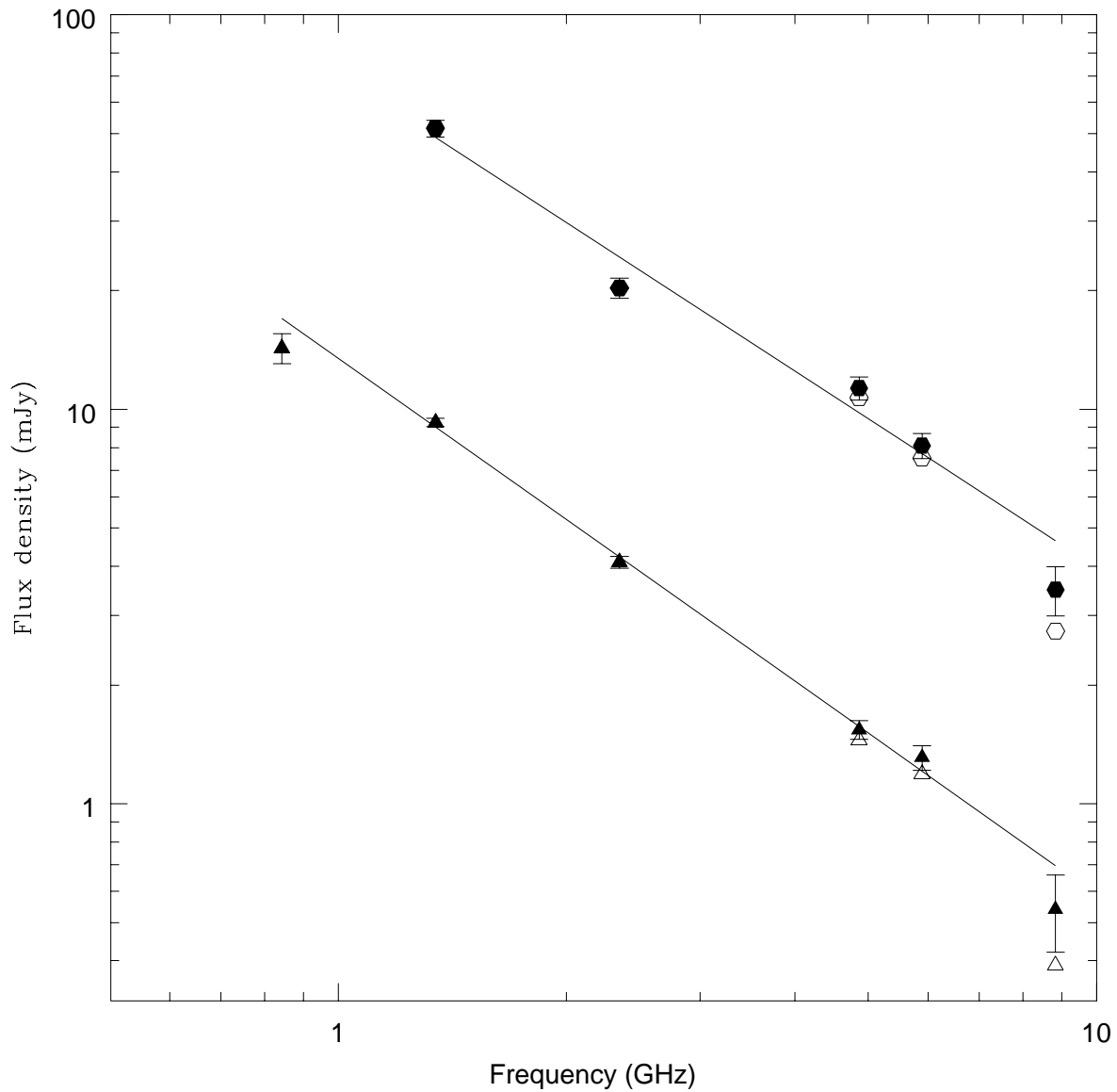
Source	Peak Position (J2000)						Flux Density (mJy)			
	h	m	s	°	'	"	S_{1344}	S_{2350}	S_{4864}	S_{8832}
A	06	58	37.9	−55	57	25	19.1 ± 1	11.8 ± 0.6	6.3 ± 0.3	3.3 ± 0.2
B	06	58	34.1	−55	57	54	0.5 ± 0.05	< 0.3	< 0.3	< 0.4
C	06	58	42.2	−55	58	37	37 ± 2	21 ± 2	8.4 ± 0.5	3.2 ± 0.5
D	06	58	23.4	−55	56	41	1.1 ± 0.06	0.4 ± 0.07	< 0.3	< 0.4
E	06	58	27.2	−55	56	08	0.4 ± 0.05	< 0.3	< 0.3	< 0.4
F	06	58	24.3	−55	55	13	0.6 ± 0.05	0.4 ± 0.07	< 0.3	< 0.4
G	06	58	19.3	−55	58	43	0.8 ± 0.05	0.4 ± 0.07	< 0.3	< 0.4
H	06	58	16.6	−55	58	23	0.4 ± 0.05	< 0.3	< 0.3	< 0.4

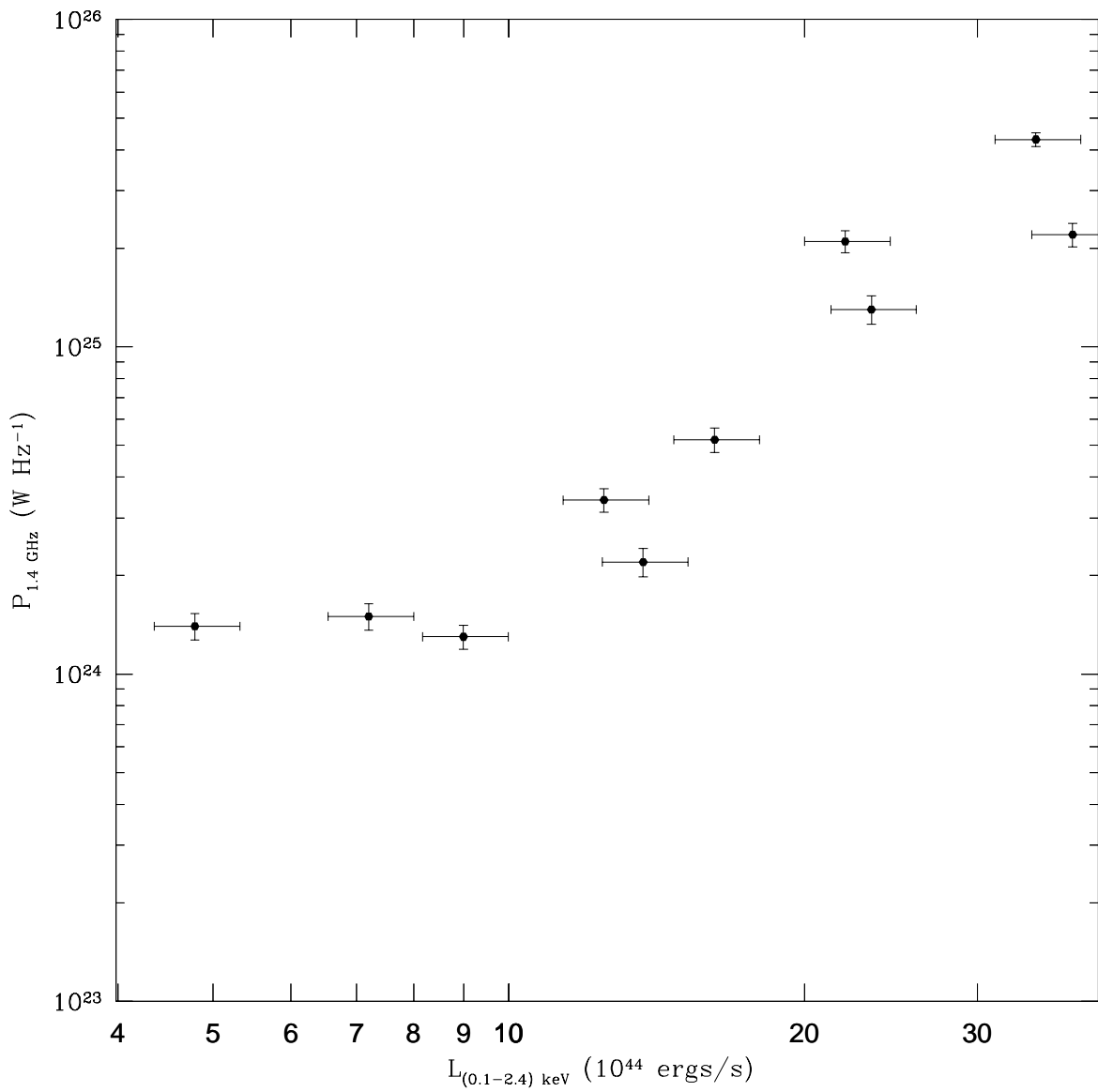
Note. — The upper limits in flux densities are 3σ , but the errors quoted are 1σ .

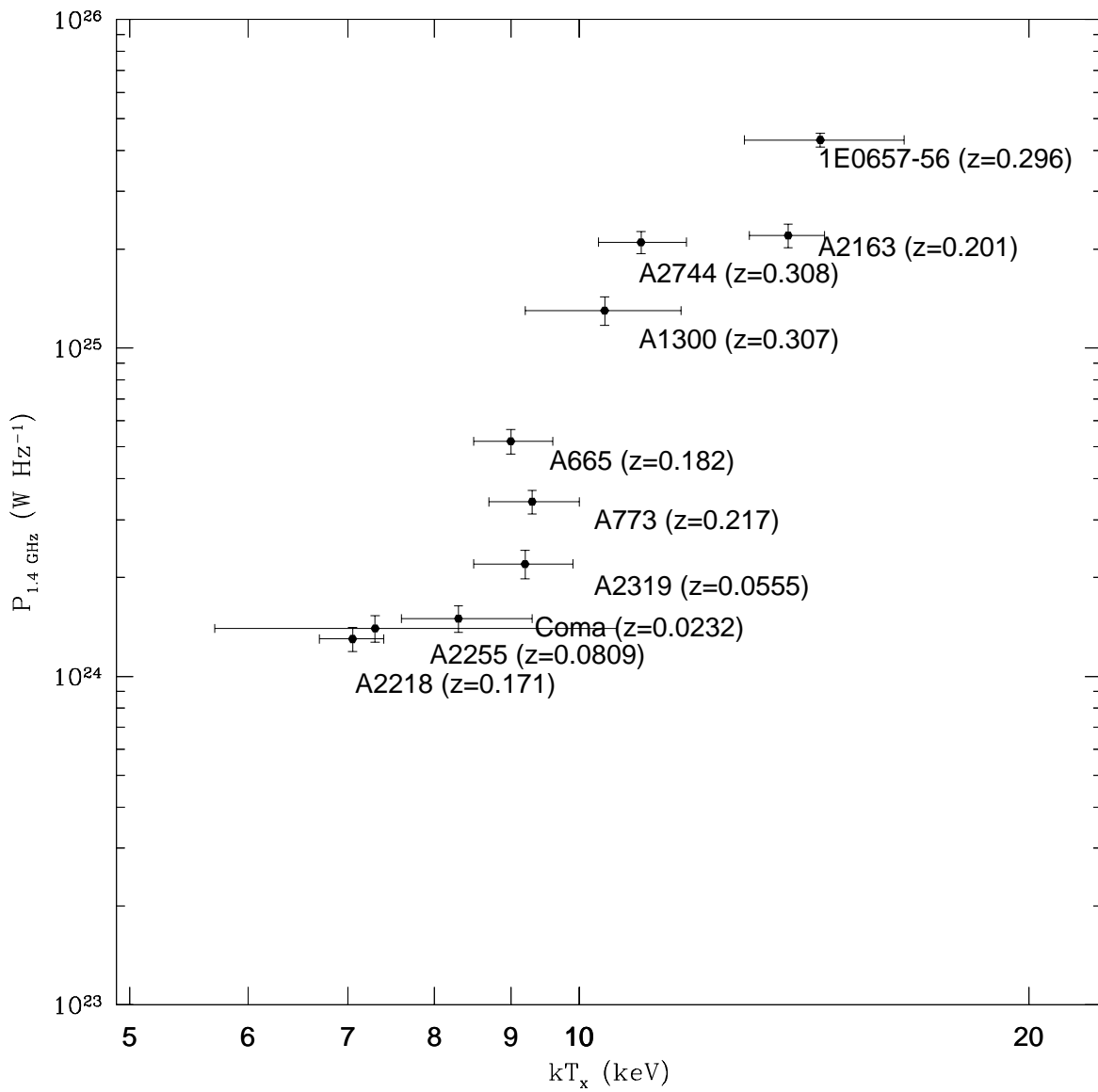












This figure "halo.rox.2.jpg" is available in "jpg" format from:

<http://arxiv.org/ps/astro-ph/0006072v1>

This figure "over.rx.jpg" is available in "jpg" format from:

<http://arxiv.org/ps/astro-ph/0006072v1>

This figure "rxjcen.jpg" is available in "jpg" format from:

<http://arxiv.org/ps/astro-ph/0006072v1>